Enhanced immunotherapy based on the synergistic click reaction-mediated chemotherapy and photothermal therapy for efficient tumor inhibition

Guiquan Zhang[1,2], Xuemei Chen[1,2], Xu Chen[1,2], Kaihong Du[1,2], Keke Ding[6], Dong He[7], Dan Ding[5], Rong Hu*[1,2,4], Anjun Qin*[1,2], and Ben Zhong Tang[2,3]

The development of functional materials for the tumor immunogenicity enhancement is desirable for overcoming the low therapeutic efficiency and easy metastasis during tumor treatments. Herein, thermos-responsive nanoparticles composed of photothermal agent (PTA) and click reactive reagent are developed for enhanced immunotherapy application. A metal-bis(dithiolene)-containing PTA with intense near-infrared (NIR) absorption and efficient photo-thermal conversion is developed for thermal-responsive nanoparticles construction. The generated heat by encapsulated PTA will further induce the phase transition of thermos-responsive nanoparticles with the release of chemotherapy reagent to react with the amino groups on functional proteins, realizing PTT and chemotherapy simultaneously. Moreover, immunogenic cell death (ICD) of cancer cells evoked by PTT will be further enhanced by the released reactive reagent. As a result, the synergistic effect of photothermal treatment and reaction-mediated chemotherapy can suppress the growth of primary tumor, and the evoked ICD will further activate the immune response with the suppression of distant tumor. This synergistic treatment strategy provides a reliable and promising approach for cancer immunotherapy in clinic.

Cancer is still a main public health issue all over the world[1]. Even with the development of treatment approaches in clinic therapy, limited treatment efficiency caused by tumor metastasis, poor targeting ability, strong side effects and easy generation of drug resistance are still needed to be overcome[2-6]. Kinds of emerging therapeutic strategies, especially multimodal treatments, have been developed to improve the treatment efficiency for tumor elimination, among which immunotherapy is attracting increasing attention because of its incomparable advantages over traditional methods by invoking immune system[7-10]. Immunotherapy based on immunogenic cell death (ICD) provides significant theoretical principle for modern cancer therapy benefited from its high efficiency towards both the primary and metastasizing tumors. Therefore, many approaches, including radiotherapy, chemotherapy, photothermal therapy (PTT) and photodynamic therapy (PDT) etc., presenting the potential of ICD inducer have been widely developed for enhanced tumor inhibition, in which the release of damage-associated molecular patterns (DAMPs) and tumor-associated antigens (TAA) will activate immune response[11-14]. The released DAMPs, such as calreticulin (CRT), high mobility group box 1 (HMGB1) protein, heat shock protein 70 (HSP70), will send the "eat me" signal to dendritic cells (DCs), resulting in DCs maturation and T cell differentiation. Meanwhile, TAA exposed on the surface of dying cells can recruit and activate tumor antigen-specific T cells to acquire eliciting antitumor immune response[15-16], achieving the effective immunotherapy.

PTT is a innovate tumor treatment modality that ablates local solid tumors by converting light to heat[17-21], and presents good antitumor behavior[22]. Various photothermal reagents (PTAs) of metal-containing nanomaterials, carbon-based nanomaterials, semiconductor polymers and low-mass molecules with near Infrared (NIR) absorption have been reported for PTT. To reduce scattering effect, PTAs locating at NIR region had attracted great attention with deeper tissue penetration depth to facilitate the therapeutic effect of PTT[23,24]. Among the PTAs, metal dithiene complexes have gained much attention and present potential as PTA for PTT application because of the intense NIR absorption, outstanding stability and tunable photophysical properties. The heat generated during PTT treatment not only can be used for ablation of solid tumors but also acts as an effective switch for drug release, providing a new platform for tumor therapy[25]. More importantly, PTT has been widely reported as an efficient inducer of ICD with the activation of immune response, and various other treatments combined with PTT were developed for tumor therapy[26,27]. However, the inhibition effect on tumor margins and metastatic tumors *in vivo* needs further improvement due to the limited effect of PTT-triggered ICD[28,29].

[1]State Key Laboratory of Luminescent Materials and Devices, Guangdong Provincial Key Laboratory of Luminescence from Molecular Aggregates, South China University of Technology, Guangzhou 510640, China. [2]Center for Aggregation-Induced Emission, AIE Institute, South China University of Technology, Guangzhou 510640, China. [3]School of Science and Engineering, Shenzhen Institute of Aggregate Science and Engineering, The Chinese University of Hong Kong, Shenzhen, 518172, Guangdong, China. Hong Kong Branch of Chinese National Engineering Research Centre for Tissue Restoration and Reconstruction, The Hong Kong University of Science & Technology, Clear Water Bay, Kowloon, Hong Kong, China. [4]School of Chemistry and Chemical Engineering, University of South China, Hengyang 421001, China. [5]State Key Laboratory of Medicinal Chemical Biology, College of Life Sciences, Nankai University, Tianjin 300071, China. [6]Department of Urology, The First Affiliated Hospital of Wannan Medical College (Yijishan Hospital of Wannan Medical College), Wuhu 241001, China. [7]Department of Urology, The First Affiliated Hospital of SooChow University, Jiangsu 215006, China. e-mail: msqinaj@scut.edu.cn; hurong@usc.edu.cn

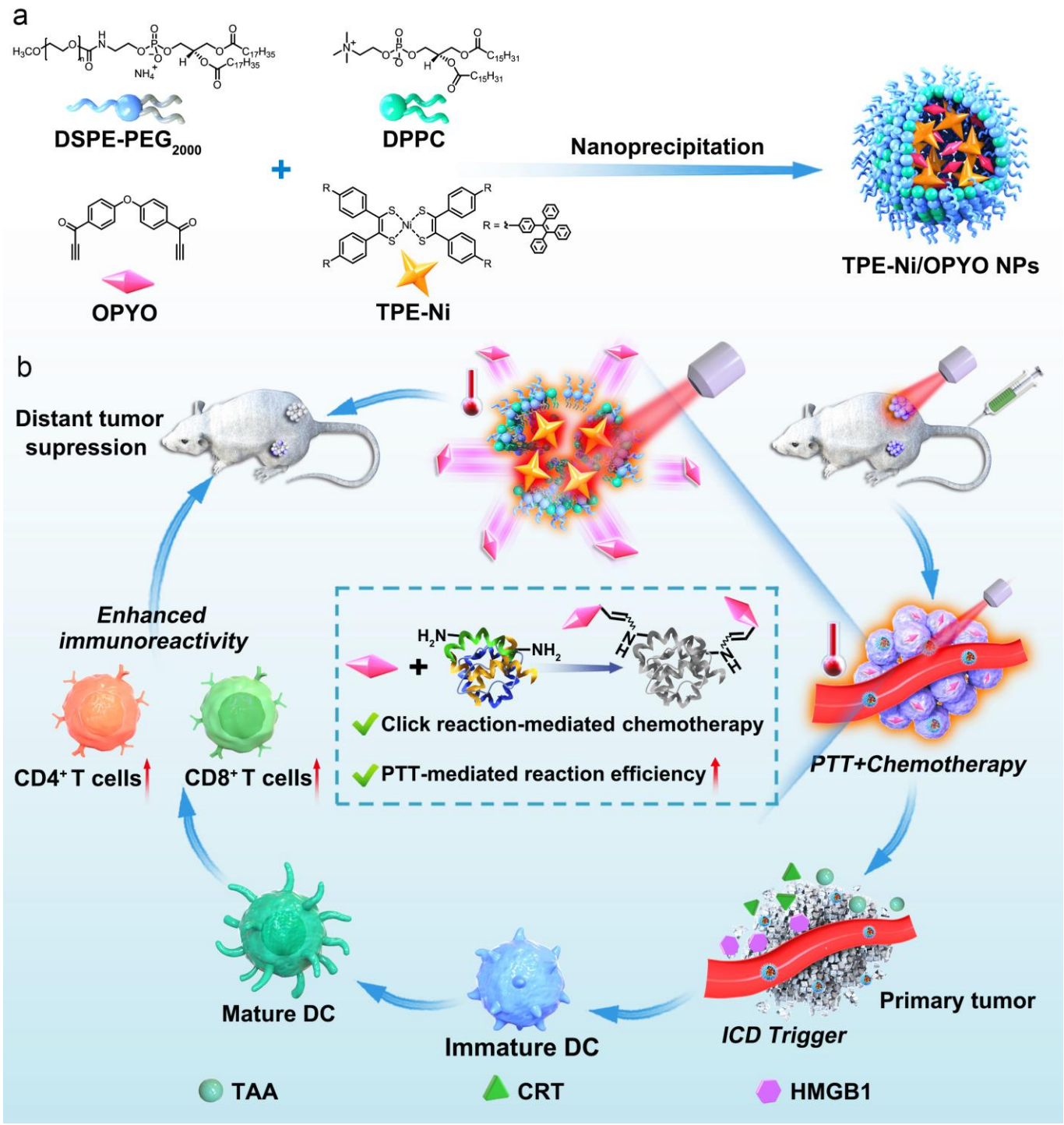

Figure 1. Schematic illustration of TPE-Ni/OPYO nanoparticles (NPs) for synergistic click reaction-mediated chemotherapy and NIR photothermal immunotherapy. a) The structure of OPYO and TPE-Ni and the preparation of TPE Ni/OPYO NPs. **b**) TPE-Ni/OPYO NPs for synergistic cancer therapy by photothermal ablation and immunogenic cell death of tumor cells.

Meanwhile, highly efficient reactions under mild reaction condition present significant promise for biomedical applications. Diverse reactions, including Staudinger ligation[30,31], quadricylane ligation[32], Diels-Alder reaction[33-35], strain promoted azide-alkyne cycloaddition (SPAAC)[36-38], Native chemical ligation (NCL)[39,40] etc, have been successfully used for bio-labeling and tracing applications. Recently, increasing reports have demonstrated the utilization of efficient reactions for therapeutic applications by disturbing or blocking the function of biomacromolecules. However, for practical applications, it is difficult to precisely regulate the efficiency, location and duration time of the reaction during practical applications. In our previous work[41], we realized the construction of “lab in cell” by using spontaneous amino-yne click polymerization, which has been successfully proven the feasibility of efficient reaction at the cellular level. However, the

selectivity towards tumor cells was relatively poor, which limits its further application in therapeutic applications.

Herein, we develop thermosensitive nanoparticles by combining click reaction and photothermal therapy for enhanced immunotherapy (Figure 1). Nickel-bis(dithiolene)-containing PTA (TPE-Ni), with intense NIR absorption was designed and developed. The functional nanoparticles were further constructed by encapsulating TPE-Ni and click reaction reagent, OPYO, by thermally responsive shell, which is composed of 1,2-dipalmitoyl-sn-glycero-3-phosphocholine (DPPC) with the phase transition temperature of 42 ^{o}C [42-44] and 1,2-distearoyl-sn-glycero-3-hosphoethanolamine-poly (ethylene glycol)-2000 (DSPE-PEG$_{2000}$) with good biocompatibility. Moreover, the constructed nanoparticles could reach 65 ^{o}C with good thermal stability after 940 nm laser irradiation, and the reactive OPYO would be sequentially released with the trigger of thermal-responsiveness by generated heat. Furthermore, the released OPYO would react with amino groups of proteins in cancer cells to achieve chemotherapy. Moreover, the photothermal effect could improve the efficiency of the click reaction. As a result, the synergetic therapy strategy based on the combination of PTT and chemotherapy could efficiently evoke ICD of cancer cells, which was more effective than the individual treatment. Furthermore, based on the enhanced permeability and retention effect (EPR) effects *in vivo*, the efficient ablation of primary tumor was achieved after the intravenous injection of nanoparticles upon 940 nm laser irradiation. Meanwhile, the generated heat would trigger the release of OPYO, which would further enhance the immunogenicity to realize the inhibition of distant solid tumors. Thus, such synergic therapy strategy with the trigger of immune response provides a reliable and innovate approach for tumor therapy in clinic.

Results

Preparation and properties of TPE-Ni/OPYO NPs

To construct PTA with high performance, we cooperate a strong acceptor of metal-bis(dithiolene) with a donor of tetraphenylethene (TPE) to provide a TPE-Ni with strong absorption in NIR region, whose synthetic route is illustrated in Figure 2a. The chemical structure of TPE-Ni and all intermediates were fully characterized (Figures S1–S3). The resultant TPE-Ni presented intense absorption in NIR region with the peak at 915 nm (Figure 2b), which is ideal candidate for PTT applications with deep tissue penetration. The functional TPE-Ni/OPYO NPs, with thermal responsibility were prepared by encapsulating PTA of TPE-Ni and the reactive agent of OPYO by DPPC and DSPE-PEG$_{2000}$. The encapsulation efficiency of TPE-Ni and OPYO were determined to be 52.7% and 4.4% by absorbance evaluation (Figure S4) and high-performance liquid chromatography (HPLC) (Figures 2c and S5), respectively. As a comparison, TPE-Ni NPs without OPYO was also prepared. As shown in Figure 2d, TPE-Ni/OPYO NPs possess a hydrodynamic diameter of 89 nm as measured by the dynamic light scattering (DLS), which was similar to that of TPE-Ni NPs and reveals that the addition of OPYO has faint effect on the nanoparticle size. The transmission electron microscopy (TEM) characterization further demonstrated the spherical morphology of both TPE-Ni/OPYO NPs and TPE-Ni NPs with the precise diameter of 53 and 56 nm, respectively (Figure S6). Such particle size is favorable for long-term circulation and further accumulation to the tumor region based on EPR effect. Moreover, under ambient conditions, TPE-Ni/OPYO NPs and TPE-Ni NPs could be stored in PBS over 28 days without any change in particle size, demonstrating the good dispersion and stability of the nanoparticles in solution (Figure 2e). And a negative surface of around –20 mV for these nanoparticles was recorded. In addition, to figure out the thermally responsive properties of the nanoparticles, the morphology was investigated by scanning electron microscope (SEM) (Figure S7), and the enlarged diameter of 90 nm was observed after heat treatment. Meanwhile, the results of DLS confirmed these properties (Figure S8). Notably, the successful release of OPYO was monitored by HPLC (Figure S9). These results verified the response towards thermal stimulation.

Thus, the photothermal property of nanoparticles was investigated systematically. First, the photothermal conversion of TPE-Ni/OPYO NPs was evaluated. The temperature of TPE-Ni/OPYO NPs solution was significantly increased to 64 ^{o}C within 10 min under the irradiation of 940 nm laser (1.0 W cm^{-2}) (Figure 2f). The photothermal conversion efficiency (PCE, η) was calculated to be 28.9% (Figure S10), which was much higher than that of ICG (17.3% [45]) and Au nanorods (21% [46]). In addition, the photothermal effect shows a laser irradiation power dependence and TPE-Ni concentration dependence, indicating that the heat generation could be well controlled (Figure S11). It is worth noting that TPE-Ni/OPYO NPs exhibits excellent photothermal stability without any change after five rapid heating/cooling cycles (Figure 2g). To evaluate the effect of heat on the reaction of OPYO with amino groups, the reaction rate of OPYO with n-propylamine was monitored in the absence and presence of TPE-Ni upon NIR laser irradiation via ReactIR. As illustrated in Figure 2h, the reaction rate was visibly accelerated in the presence of TPE-Ni upon NIR irradiation with the constant k value of 0.15 M^{-1}S^{-1} compared to that of control group (k = 0.06 M^{-1}S^{-1}). The result demonstrated that OPYO could react with amino groups spontaneously, which would be further accelerated by increasing the temperature. Thus, we can conclude that the high reaction ability of OPYO shows high potential for chemotherapy upon releasing, and the synergistic treatment effect can be achieved based on PTT.

In addition, biocompatibility is one of the prerequisites of a PTA for the clinical application. Therefore, the standard Cell Counting Kit-8 (CCK-8) assay was firstly used to assess the cytotoxicity of TPE-Ni/OPYO NPs and TPE-Ni NPs without light irradiation. After co-incubation for 24 h, the cell viability of murine breast cancer cells (4T1 cell) presented relatively weak change compared with the blank group, which proved that both TPE-Ni/OPYO NPs and TPE-Ni NPs had good biocompatibility (Figure 2i). In addition, hemolysis experiments also supported their excellent biosafety, assuring their therapeutic application *in vivo* (Figure 2j).

Cellular phototoxicity and NIR induced ICD

To evaluate the therapeutic effect, the phototoxicity of TPE-Ni/OPYO NPs and TPE-Ni NPs towards 4T1 cancer cells were examined (Figure 3a). Upon irradiation with 940 nm laser for 5 min, as expected, the survival rate of 4T1 cell decreased significantly with the increase in the concentration of nanoparticles. Meanwhile, the survival rate of cells incubated with TPE-Ni/OPYO NPs was much lower than that of TPE-Ni NPs within the concentration range of 20~40 μg mL^{-1}.

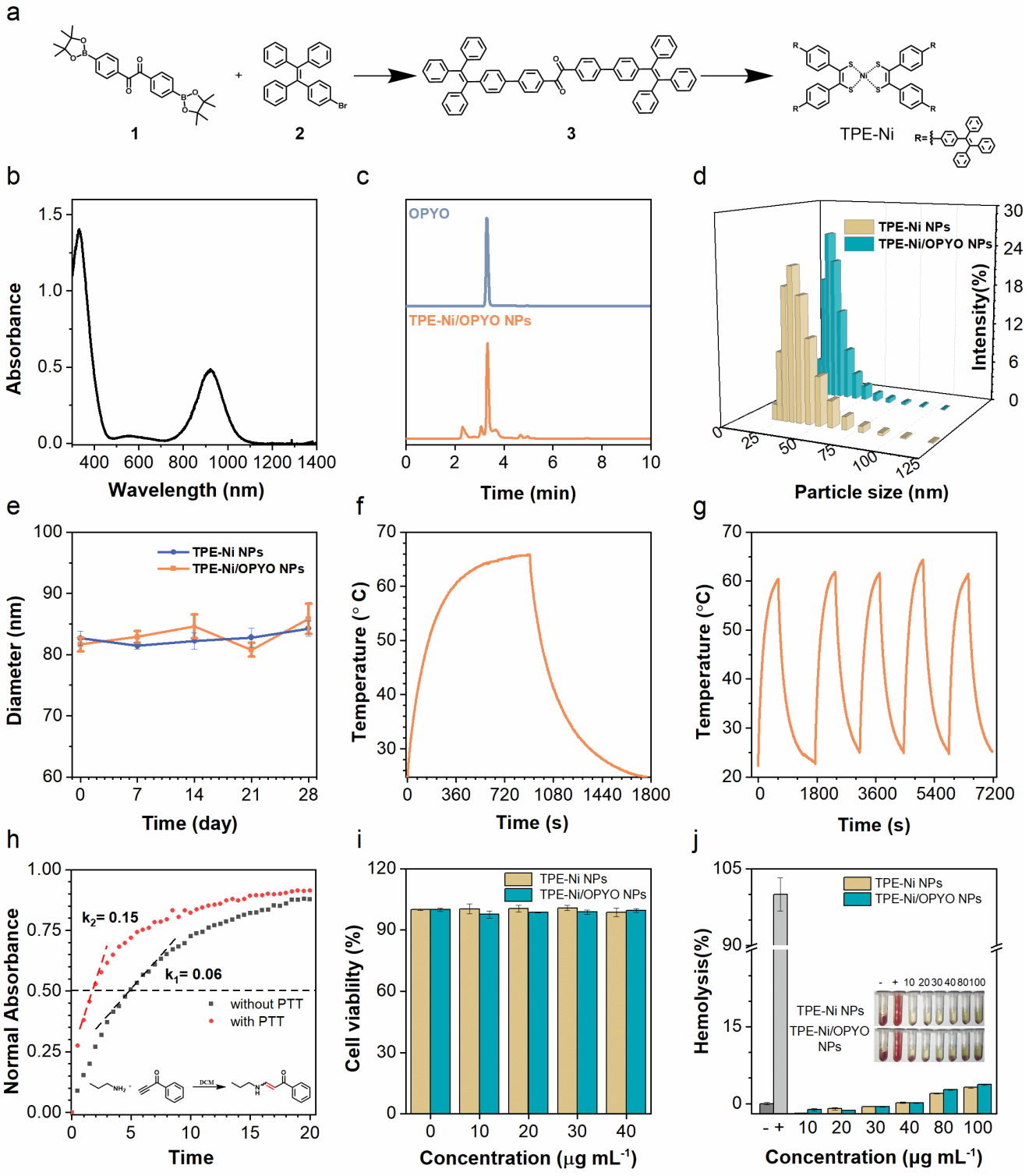

Figure 2. Preparation and properties of TPE-Ni/OPYO NPs and TPE-Ni NPs. **a**) Synthetic route of TPE Ni. **b**) Ultraviolet (UV)/visible (Vis)-NIR absorption spectra of TPE-Ni. **c**) Determination of OPYO encapsulation in TPE-Ni/OPYO NPs by HPLC. **d**) Size distribution of TPE-Ni/OPYO NPs and TPE-Ni NPs. **e**) Diameter variation of TPE-Ni/OPYO NPs and TPE-Ni NPs during 28 days. **f**) Photothermal temperature curves of TPE-Ni/OPYO NPs(100 μg mL^{-1}, 940 nm, 1.0 W cm^{-2}). **g**) Photothermal stability measurement of TPE-Ni/OPYO NPs (100 μg mL^{-1}, 940 nm, 1.0 W cm^{-2}). **h**) The time-dependent peak intensity of *in situ* FT-IR profiles at 1633 cm^{-1} with or without laser. **i**) Cell viabilities of 4T1 cells after incubation with TPE-Ni/OPYO NPs or TPE-Ni NPs with different concentrations. **j**) Hemolysis assay of TPE-Ni/OPYO NPs and TPE-Ni NPs.

The enhanced inhibition behavior towards cancer cells is due to the successful release of OPYO based on the photothermal responsiveness, which will disturbing and blocking the functions of intracellular biomolecules by reacting with the related amino groups. These results indicated the synergetic therapy effect of PTT and chemotherapy based on PTA and OPYO. To facilitate the visualization of the phototherapeutic effect of NPs, calcein AM and propidium iodide (PI) were used for live/dead cell staining imaging. After laser irradiation, cells in blank group were all well stained by calcein AM with bright green fluorescence (Figure 3b), indicating that the laser alone exhibited faint effect on the proliferation of 4T1 cells under this condition.

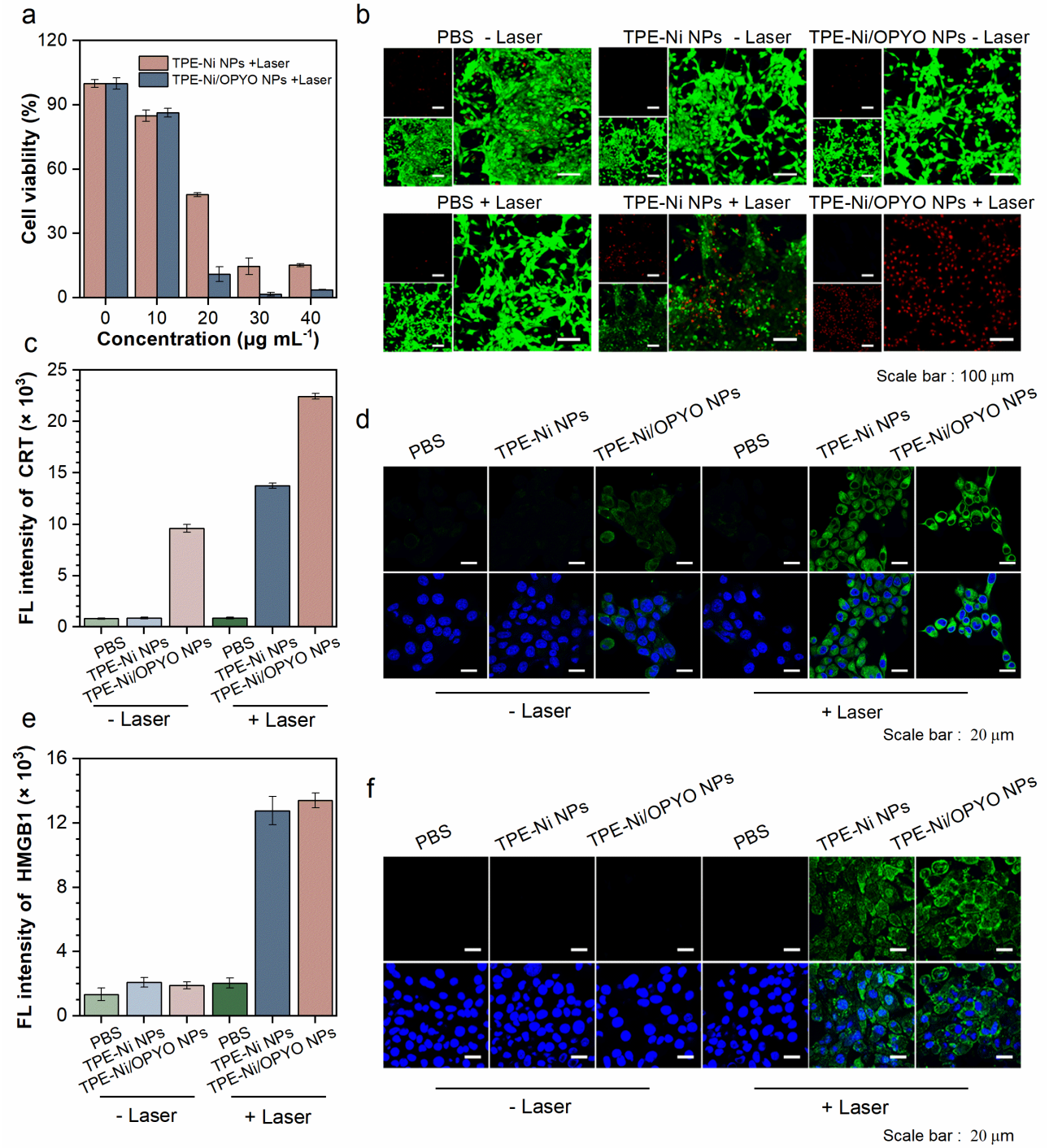

Figure 3. ***In vitro*** **NIR PTT induced cellular phototoxicity and ICD. a**) Cell viabilities of 4T1 cells after incubation with different treatments (940 nm, 1.0 W cm^{-2}, 5 min). **b**) CLSM images of 4T1 cells co-stained with calcein-AM (green fluorescence) and PI (red fluorescence) after various treatments. **c**) Quantitative analyses of CRT expression levels and **d**) CLSM images of 4T1 cells with immunofluorescence staining of CRT (green fluorescence) after different treatments. **e**) Quantitative analyses of HMGB1 expression levels and **f**) CLSM images of 4T1 cells with immunofluorescence staining of HMGB1 (green fluorescence) after different treatments.

Whereas, for the cells incubated with TPE-Ni NPs, fractional red fluorescence from PI was detected, along with the green fluorescence from calcein AM, indicating that it was difficult to efficiently kill all 4T1 cells under this condition. Notably, under the same experimental conditions, almost no green fluorescence signal was observed for cells treated by TPE-Ni/OPYO NPs with near-infrared laser irradiation, which verified the synergetic therapy effect of TPE-Ni triggered PTT and OPYO-mediated chemotherapy.

After verifying the efficient ablation of cancer cells, we further investigated the potential of TPE-Ni/OPYO NPs in immunotherapy. ICD related biomarkers for cells with different treatment were evaluated. As mentioned above, the appearance of CRT on the cell membrane and the high expression of HMGB1 protein are typical features of ICDs, which will generate the signal of "eat me" and further enhance the uptake of tumor antigens and antibody expression by DCs to activate immune response[47,48].

As shown in Figure 3c and 3d, with the utilization of immunofluorescence analysis, both TPE-Ni NPs and 940 nm laser irradiation could not induce the expression of CRT on 4T1 cells surface. And faint green fluorescence could be observed for cells treated with TPE-Ni/OPYO NPs without laser irradiation, which demonstrated that the high reactivity of OPYP with functional biomolecules could induce the expression of CRT to some extent. Increased CRT expression was acquired for cells with TPE-Ni NPs treatment upon exposure to 940 nm laser. Meanwhile, the most intense green fluorescence was observed for cells incubated with TPE-Ni/OPYO NPs for 12 h with 940 nm laser irradiation, indicating a high level of CRT expression induced with the synergetic activation effect of chemotherapy and PTT. The remarkable difference could also be visually observed in fluorescence

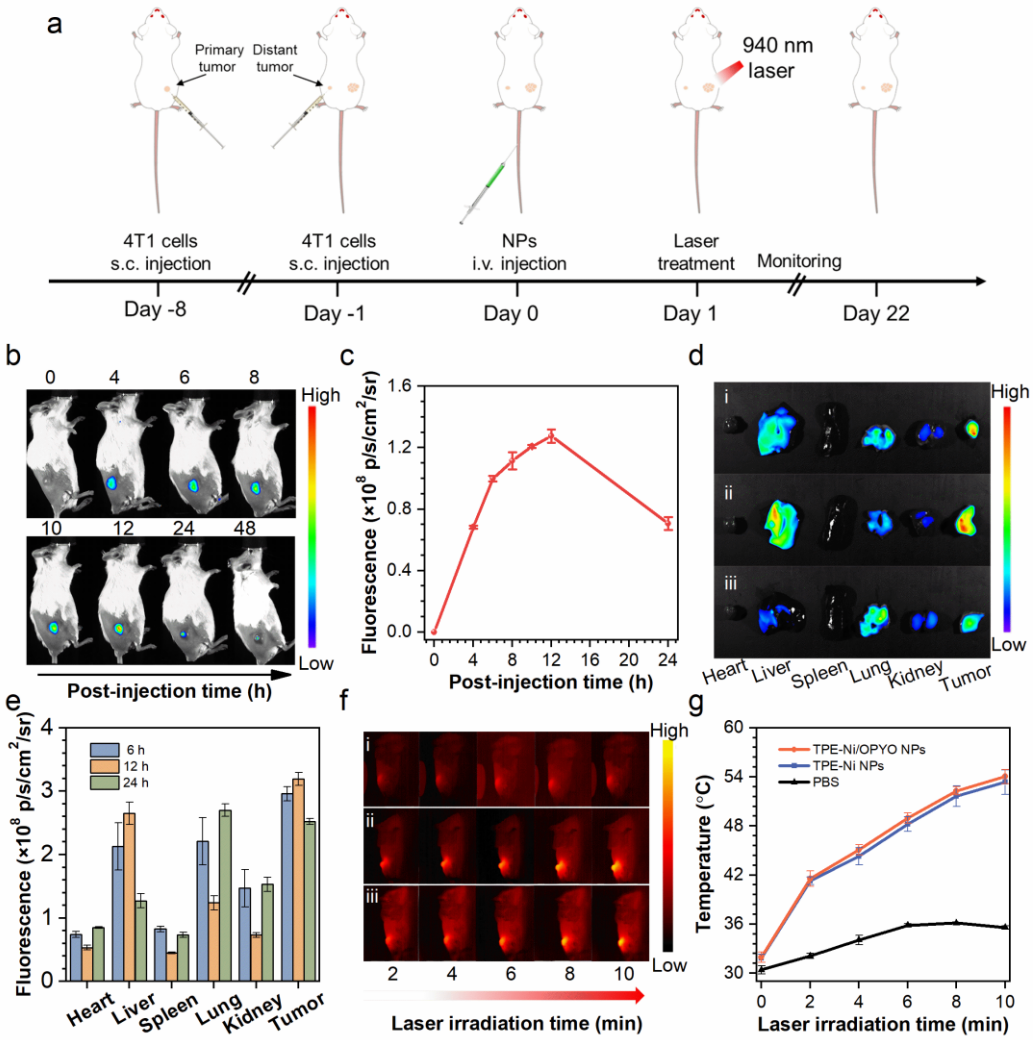

Figure 4. Schematic of time schedule for cancer therapy. *In vivo* NIR fluorescence imaging and photothermal imaging. a) Treatment schedule for *in vivo* antitumor study.b) *In vivo* NIR fluorescence imaging of primary tumor in 4T1-tumor-bearing mice after intravenous injection of TPE-Ni/OPYO/TT-TBZ NPs (0.15 mL, the concentration of TPE-Ni = 250 μg mL^{-1}) at different time, n = 3. $\lambda_{ex}/\lambda_{em}$ = 620 nm/840 nm. **c**) The corresponding fluorescence intensity of **b**). **d**) *Ex vivo* NIR fluorescence imaging of dissected main organs and primary tumors of the mice sacrificed post intravenous injection of TPE-Ni/OPYO/TT-TBZ NPs, n = 3. $\lambda_{ex}/\lambda_{em}$ = 620 nm/840 nm (i : 6 h, ii : 12 h, iii : 24 h). **e**) The corresponding fluorescence intensity of **d**). **f**) Thermal imaging of 4T1-tumor-bearing mice under laser irradiation (940 nm, 1.0 W cm^{-2}, 10 min) at 12 h after intravenous injection of PBS (i), TPE-Ni NPs (ii) or TPE-Ni/OPYO NPs (iii), n = 3. **g**) The corresponding temperature of **f**).

intensity statistical analysis, and the mean fluorescence intensity of CRT staining for cells treated with TPE-Ni/OPYO NPs without and with NIR light irradiation were about 17- and 28-times higher than that of the blank group, respectively. Moreover, the expression of HMGB1 was studied as well (Figure 3e and 3f), and the results showed that PTT treatment could successfully upregulate the expression of HMGB1. However, no enhancement could be detected in the group incubated with TPE-Ni/OPYO NPs without NIR light irradiation, revealing that OPYO presented negligible effect on upregulation of HMGB1 expression. These results clearly demonstrated that TPE-Ni/OPYO NPs-mediated chemotherapy and PTT could provoke the ICD of cancer cells and further activate the immune response for the potential application of immune therapy.

In vivo fluorescence imaging biodistribution and photothermal imaging

Given to the satisfactory results of ICD activation at cellular level, we further evaluated the tumor inhibition ability based on TPE-Ni/OPYO NPs *in vivo*. As show in Figure 4a, mouse models were constructed by subcutaneous injection of 4T1 cells in the bilateral hips of female BALB/c mice on the -8 and -1 day, respectively. The first and second inoculated tumors were employed to establish primary and distant tumors. To figure out the optimal accumulation time in primary tumors and NPs distribution *in vivo* by fluorescence monitoring, a luminogen of TT-TBZ was designed and synthesized (Figures S12-S14). Photophysical properties investigation demonstrated that TT-TBZ showed the maximum absorption at 600 nm and NIR emission at 905 nm (Figure S15), which is desirable for *in vivo* applications. Moreover, the emission of TT-TBZ in THF/water mixtures with different water fraction (f_w) was studied (Figure S16), in which the fluorescence decreased at first when f_w values are below 50% because of the twisted intramolecular charge transfer (TICT) process. Afterward, the emission apparently increased indicating that TT-TBZ possessed the unique aggregation-induced emission (AIE) feature[49].

Thanks to the AIE feature of TT-TBZ, the fluorescent nanoparticles were obtained by doping it into non-fluorescent TPE-Ni/OPYO NPs (Figure S17). The experiments showed that the sizes of the constructed TPE-Ni/OPYO/TT-TBZ NPs was similar to that of TPE-Ni/OPYO NPs (Figures S18 and S19) and the encapsulation efficiency of TT-TBZ was 65.4% (Figure S20). By employing the NIR emission of TT-TBZ, the *in vivo* enrichment and distribution behavior of nanoparticles were

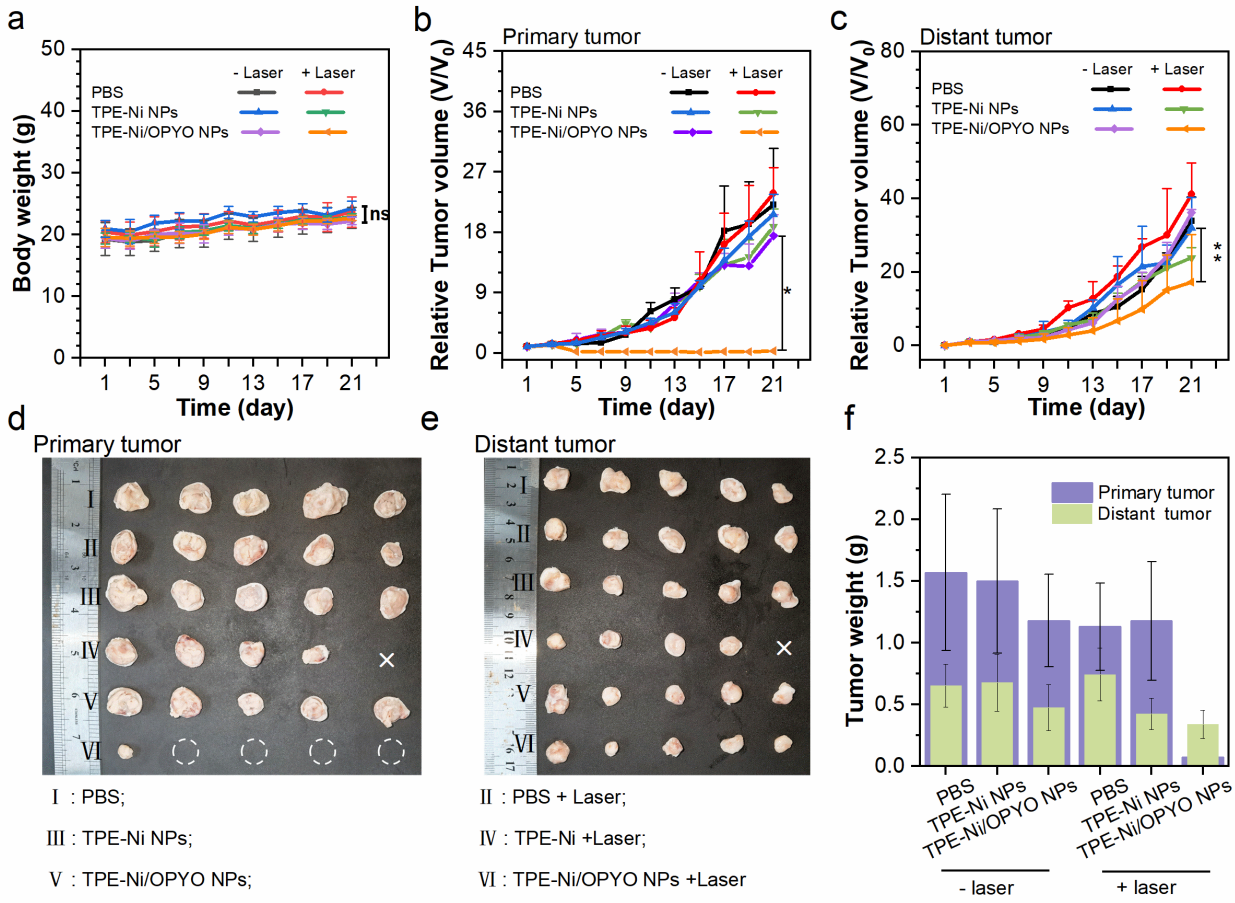

Figure 5. Anti-tumor efficacy of TPE-Ni/OPYO NPs and TPE-Ni NPs. a) Body weight of of 4T1-tumor-bearing mice with different treatments. **b**) Relative primary tumor volume changes of 4T1-tumor-bearing mice with different treatments, n = 5. **c**) Relative distant tumor volume changes of 4T1-tumor-bearing mice with different treatments, n = 5. **d**) Excised primary tumors after different treatments. **e**) Excised distant tumors after different treatments. **f**) Primary and distant tumors weight of 4T1-tumor-bearing mice with different treatment. *p = 0.018 (**b**), **p = 0.003 (**c**) were tested by using ANOVA.

explored. As shown in Figure 4b, after systemic administration, the fluorescence intensity in the tumor region increased gradually and reached maximum at 12 h with the signal-to-noise (S/N) ratio of 5, demonstrating effective accumulation of nanoparticles in tumors (Figure 4c). Thereafter, mice were sacrificed and the distribution of nanoparticles were studied by measuring *in vitro* fluorescence signals of major organs and tumor tissues at different time points after tail-vein injection. By analyzing the fluorescence intensity, it was found that nanoparticles were primarily accumulated in the tumor and liver, then the enrichment in lung and kidney could be detected (Figure 4d and 4e). Interestingly, considerable fluorescence was observed in lungs, which was proved to be the tumor metastasis (Figure 4d). These results verified the high selectivity of nanoparticles to solid tumor *in vivo*.

Meanwhile, the photothermal efficacy of TPE-Ni/OPYO NPs was also evaluated at mice primary tumors *in vivo*. After tail-vein injection for 12 h, the primary tumor was irradiated with 940 nm laser (1.0 W cm^{-2}) for 10 min, and the temperature of tumor region was recorded by infrared thermos-imaging camera (Figure 4f). As shown in Figure 4g, compared with the blank group, significant enhancement of temperature in TPE-Ni/OPYO NPs-treated tumor region could reach to 54 °C, demonstrating the efficient photothermal ability and high promise for PTT application *in vivo*.

Effectiveness of TPE-Ni/OPYO NPs and TPE-Ni NPs in the treatment of primary tumors and distant tumors *in vivo*

Furthermore, to evaluate the tumor inhibition effect towards distant metastases *in vivo*, the tumor growth and weight changes of mice with different treatments were monitored for 21 days, respectively. Compared with the blank group, the body weight of mice in all experimental groups didn't change significantly, indicating that both nanoparticles and light irradiation could not cause any damage to the mice (Figure 5a). After verifying the good biosafety, the growth of primary tumors and distant tumors in different groups were recorded. As shown in Figure 5b and 5c, both the primary tumors and the distant tumors growth of mice with TPE-Ni NPs treatment was similar to that of blank group, suggesting that TPE-Ni alone impacts negligible effect on tumor suppression. Even though the incorporation of OPYO would improve ablation efficiency towards both the primary tumors and the distant tumors, the *in vivo* inhibition effect was not desirable. Furthermore, by introducing NIR laser irradiation to activate photothermal effect, the growth of primary and distant tumors for mice injected with TPE-Ni NPs was partly inhibited. Delightfully, for TPE-Ni/OPYO NPs-treated group, the primary tumors were fully eradicated, and 68% of the distant tumor growth was inhibited at the same time, demonstrating the high efficiency of tumor inhibition. Afterward, both primary and distant tumors were collected and weighed (Figure 5d-5f), which showed the similar trend to that of tumor volumes with different treatments.

Moreover, hmatoxylin-eosin (H&E) staining was employed to reveal the mechanism of cell death in primary and distant tumors in all groups. The results indicated that the apoptosis and necrosis of cancer cells were more severe in mice treated with TPE-Ni/OPYO NPs than those of TPE-Ni NPs treated mice in the presence of laser irradiation, while no significant cell death was found in other groups (Figure S21). The H&E staining of the major organs was also obtained and no damage was found, indicating that the nanoparticles have good biocompatibility (Figure S22). Furthermore, TdT-mediated dUTP Nick-End Labeling (TUNEL) staining demonstrated that nanoparticles inhibited the growth of distant tumors through the apoptotic pathway (Figure 6a). These results demonstrate that this synergetic therapy approach possesses outstanding tumor inhibition effect with desirable biosafety.

Anti-tumor immune mechanism

To essentially figure out the underlying mechanism of the anti-tumor and anti-metastatic efficacy, two of the most important factors in immunotherapy[50,51], the maturation of DCs and activation of immune cells, were investigated and analyzed. Along this line, tumor-draining lymph nodes of mice were selected to analyze the maturation of DCs by flow cytometry (Figures 6b and S23). Compared with blank group, the populations of mature DCs ($CD86^+$ $CD11C^+$) increased by 89.9% and 38.3% in the group of TPE-Ni/OPYO NPs and TPE-Ni NPs with laser irradiation, respectively. Meanwhile, the populations of mature DCs did not change significantly in the absence of laser irradiation, suggesting that both OPYO-mediated click reaction and photothermal effect had a significant effect on the triggering of DCs maturation. The mature DCs can further contact, phagocytose and present antigens to nascent T cells, which subsequently differentiate into effector T cells, such as $CD3^+CD4^+$ helper T lymphocytes (HTL) and $CD3^+CD8^+$ cytotoxic T lymphocytes (CTL)[52]. Thus, we further investigated the activation of T lymphocytes in distant tumors and spleens. Compared with the blank group, the percentage of $CD3^+CD8^+$ CTLs in the distant tumor tissues of mice increased from 9.63% to 22.3% based on the treatment of TPE-Ni/OPYO NPs in the presence of laser irradiation, meanwhile, the percentage of $CD3^+CD4^+$ HTLs raised from 13.15% to 37.3% (Figure S24). Moreover, under the same treatments, the percentages of $CD3^+CD8^+$ CTLs and $CD3^+CD4^+$ HTLs in spleen tissues reached 19.53% and 46.86%, respectively (Figures 6c and S25). These results verified that PTT treatment based on TPE-Ni/OPYO NPs could efficiently activate immune response and displayed great promise for immunotherapy.

Natural killer T cells (NKTs) are a type of special immune cells which act as a "bridge" between innate and adaptive immunity[53], in which NKTs simulated by tumor antigens will secrete cytokines (e.g., Th1 and Th2) simultaneously to regulate the immune system[54]. Therefore, the blood of mice with different treatments were measured by flow cytometry to study the changes of NKTs (Figure S26). In the TPE-Ni/OPYO NPs-injected group with laser irradiation, the populations of NKTs in the blood were 1.40-fold higher than the corresponding blank group. Moreover, several tumor immune-related factors, including tumor necrosis factor-α (TNF-α), interferon-γ (IFN-γ) and interleukin-6 (IL-6), in the blood were also measured

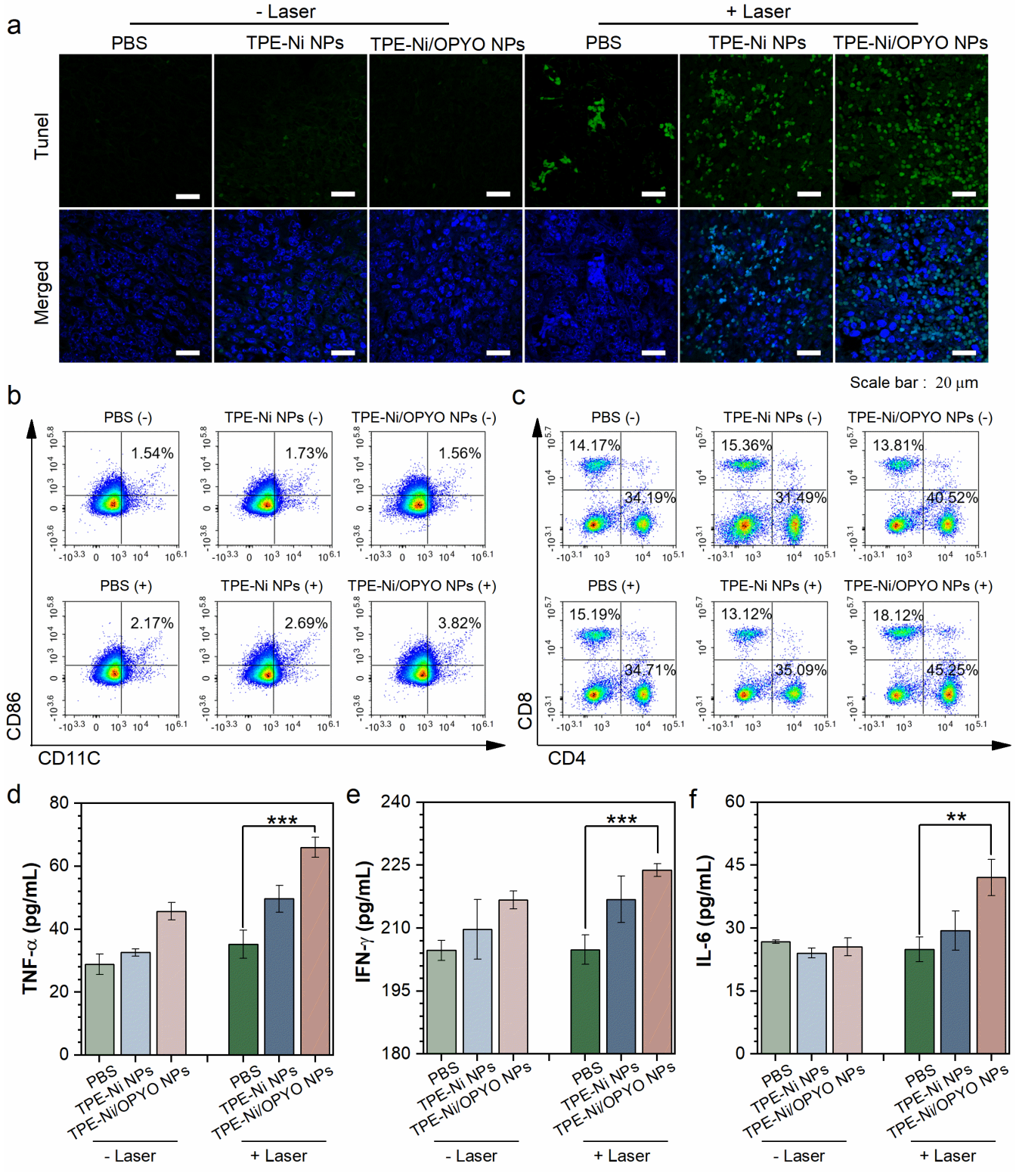

Figure 6. ***In vivo*** **click reaction and NIR PTT induced tumor cell apoptosis, DC maturation and activation of immune response. a**) Tunel staining of the distant tumors after different treatments. **b**) DCs in tumor-draining lymph nodes after different treatments, n = 4. **c**) $CD3^+CD8^+$ T cells and $CD3^+CD4^+$ T cells in spleen after different treatments, n=4. **d-f**) Blood serum levels of TNF-α (**d**), IFN-γ (**e**) and IL-6 (**f**) in 4T1-tumor-bearing mice after different treatments. ***p = 0.0001 (**d**), ***p = 0.001 (**e**), **p = 0.002 (**f**).

using enzyme linked immunosorbent assay (ELISA) (Figure 6d-6f). Increased expression of all three cytokines was observed in the blood of mice treated by TPE-Ni/OPYO NPs with laser irradiation, which was more effective than that of mice treated

with TPE-Ni NPs. These results indicate that the synergetic therapy strategy was highly desirable for tumor inhibition, regardless of primary or distant tumors. Thus, the mechanism of anti-tumor and anti-metastasis effect based on this strategy is proposed as follows: the generated heat by TPE-Ni under laser readily activates the phase transition of nanoparticles to release OPYO. As a result, the PTT and reactivity of OPYP induce ICD of tumor cells together and further enhance the immune response both *in vitro* and *in vivo*. The synergetic therapy effect is much better than that of individual treatment through efficiently promoting the maturation of DCs and further activation of immune therapy.

Biocompatibility evaluation of TPE-Ni/OPYO NPs and TPE-Ni NPs

Finally, blood routine analysis and biochemical analysis were used to evaluate the biosafety of nanoparticles *in vivo* after systemic administration. And the results of the analysis showed that the parameters were generally consistent with those of the blank group (Figure S27). Major organs, including heart, liver, spleen, lung and kidney, were collected for histopathological observation by H&E staining (Figure S28). The results showed no damage to the major organs by nanoparticles which means the excellent biocompatibility. These results indicated that the spatiotemporal selective release of chemotherapy agent by NIR laser is essentially promise for tumor immunotherapy in clinic.

Discussion

In this work, a new synergetic therapy strategy of tumor immunotherapy with high biosafety and desirable therapy efficiency by thermal-responsive nanoparticles containing NIR PTA and chemotherapy regent was established. The encapsulated photothermal agent of TPE-Ni can not only be used for PTT but also induce the release of chemotherapy agent of OPYO by triggering the thermos-response of nanoparticles. In the meantime, the efficiency of the click reaction can be significantly enhanced by the photothermal effect. It has been verified that the enhanced killing effect and activation of ICD were achieved compared with the individual treatments based on this synergetic therapeutic method. Furthermore, significant inhibition of both primary and distant tumors was realized by evoking body immunity *in vivo*, which is difficult to achieve by photothermal therapy. This synergetic therapy strategy provides a reliable and promising platform for tumor treatment in clinic applications.

Methods

Synthesis of TPE-Ni

For detailed synthesis procedure, please refer to supplementary data.

Preparation of nanoparticles

TPE-Ni (1.0 mg), OPYO (1.0 mg), DPPC (25 mg) and DSPE-PEG_{2000} (25 mg) were dissolved in 5 mL of THF/chloroform (v/v, 4:1) mixture under ultrasonic dispersion. Then the homogeneous mixture was quickly added into ultrapure water (9 mL). After sonication using a probe sonicator at 30% output for 3 min, the mixture was purified by dialysis (molecular weight cut-off 3.5 KDa) for 2 days to eliminate the organic solvent and unloaded molecules. Then the NPs were collected and concentrated by centrifugal filters for further use. The obtained TPE-Ni/OPYO NPs was stored at 4 °C. TPE-Ni NPs and TPE-Ni/OPYO/TT-TBZ NPs were also prepared using the same method. The Shimadzu UV-2600 spectrophotometer and high-performance liquid chromatography (HPLC) were used to determine the concentrations of TPE-Ni and OPYO in nanoparticles. The encapsulation efficiency (EE) was calculated according to the following formula:

$$\mathrm{EE} = \frac{\text{loading amount}}{\text{feeding amount}} \times 100\%$$

Photothermal release of OPYO *in vitro*

Water solutions of TPE-Ni/OPYO NPs were exposed to 940 nm laser for different time (20, 40 and 60 min). Subsequently, the precipitate was collected using an ultrafiltration centrifugal tube (Millipore, MWCO10 kD). Then, acetonitrile was added into the precipitate. The mixed solution was filtrated through a 0.22 μm polyvinylidene fluoride syringe driven filter (Millipore, Millex-GP) and then used for HPLC analysis (eluent: acetonitrile, detection wavelength: 320 nm).

***In vitro* photothermal study**

For the purpose of evaluating the photothermal ability of TPE-Ni, the effect of the power density and the concentration of NPs on the conversion efficiency were studied.

Effect of the power density: 200 μL of TPE-Ni/OPYO NPs or TPE-Ni NPs (the concentration of TPE-Ni = 100 μg mL^{-1}) were irradiated by 940 nm laser at different power densities (0.2, 0.4, 0.6, 0.8 and 1.0 W cm^{-2}). Solution temperature was monitored every 1 s by the IR thermal camera.

Effect of the concentration: different TPE-Ni concentrations of TPE-Ni/OPYO NPs or TPE-Ni NPs were prepared (the concentration of TPE-Ni = 20, 40, 60, 80 or 100 μg mL^{-1}), and irradiated by 1.0 W cm^{-2} of 940 nm laser. The temperature change was monitored during irradiation.

To evaluate the photothermal stability of nanoparticles, the heating and cooling were repeated for five cycles.

To measure the photothermal conversion efficiency, TPE-Ni/OPYO NPs or TPE-Ni NPs (the concentration of TPE-Ni = 100 μg mL^{-1}) were exposed to 940 nm irradiation at the density of 1.0 W cm^{-2} for 15 min to reach the thermal equilibrium, and then the solution was cooled to room temperature. The temperature of the solution was recorded at an interval of 1 s during this process. The photothermal conversion efficiency (η) was measured according to the following formula:

$$\eta = \frac{hs(T_{Max} - T_{Surr}) - Q_s}{I(1 - 10^{-A_{940}})}$$

where, h is the heat transfer coefficient; s is the surface area of the container. Q_s is light absorbance of solvent, I is the laser energy for the 940 nm laser, and A_{940} is related to the absorbance value of the TPE-Ni/OPYO NPs or TPE-Ni NPs tested by analysis of the UV-Vis spectrum at 940 nm.

$$hs = \frac{mC_{water}}{\tau_s}$$

where, m is the mass of the solution containing the NPs, C_{water} is the specific heat capacity of the solution (C_{water} = 4.2 J g^{-1} K^{-1}), and τ_s is the associated time constant, which is calculated from the linear time-dependent data collected in the cooling period.

$$t = -\tau_s \ln \theta$$

θ is a dimensionless parameter, known as the driving force temperature.

$$\theta = \frac{T - T_{Surr}}{T_{Max} - T_{Surr}}$$

where, T_{max} and T_{Surr} are the maximum steady state temperature and the environmental temperature, respectively.

Cell culture and cytotoxicity test

4T1 cells were cultured in DMEM with 10% FBS and 1% antibiotics (penicillin and streptomycin) in an atmosphere containing 5% CO_2 and 95% humidified air at 37 ˚C. The cells

were seeded into 96-well cell culture plates at a density of 1 × 10^4 cells/well and cultured for 24 h, followed by treatment with TPE-Ni/OPYO NPs or TPE-Ni NPs at different TPE-Ni concentrations (0, 10, 20, 30 and 40 μg mL^{-1}) for another 24 h. Then the culture medium was removed and cells were gently washed by fresh 1×PBS. 100 μL fresh DMEM together with 10 μL CCK-8 solution was then added to each well and cells were then incubated for 2 h. To calculate the cell viability, the absorption was recorded by a microplate reader at 450 nm after shaking for 2 min. The cell viability ratio (VR) was evaluated according to the following equation:

$$VR = \frac{A}{A_0} \times 100\%$$

where A_0 is the absorbance of cells without any NPs, and A is the absorbance of cells incubated TPE-Ni/OPYO NPs or TPE-Ni NPs.

Hemolysis assay

Hemolysis assays were conducted to assess the in vivo toxicity of TPE-Ni/OPYO NPs and TPE-Ni NPs. Briefly, red blood cells were harvested from healthy BALB/c mice, centrifuged at 2000 rpm for 3 min and the serum removed using a syringe. Cells were washed five times with 1 × PBS solution and suspended in 1 × PBS solution. The diluted red blood cells suspension (0.2 mL) was then mixed with 0.8 mL of various samples: PBS as a negative control, ultrapure water as a positive control and different concentrations of TPE-Ni/OPYO NPs or TPE-Ni NPs in PBS solution (final TPE-Ni concentrations: 10, 20, 30, 40, 80 and 100 μg mL-1, final OPYO concentrations: 0.83, 1.67, 2.50 ,3.34, 6.68 and 8.35 μg mL-1). Subsequently, the mixtures were vortexed and rested for 2 h at 37 °C. Mixtures were then centrifuged at 15,000 rpm for 10 min to precipitate erythrocytes. The absorbance at 540 nm recorded by a microplate reader.

Nanoparticles stability test

TPE-Ni/OPYO NPs and TPE-Ni NPs were dispersed in 1× PBS (2 mL) at TPE-Ni concentration of 40 μg mL-1, respectively. Then the hydrodynamic diameters were determined by DLS every 7 days.

***In vitro* photothermal therapy (PTT) studies**

The 4T1 cells were seeded into 96-well cell culture plates at a density of 1 × 104 cells/well and cultured for 24 h, followed by treatment with TPE-Ni/OPYO NPs or TPE-Ni NPs at different TPE-Ni concentrations (0, 10, 20, 30 and 40 μg mL-1) for another 12 h. Subsequently, the cells were washed three times with PBS and irradiated (940 nm, 1.0 W cm-2) for 5 min and further incubated for another 12 h. Then the culture medium was removed and 100 μL of fresh DMEM together with 10 μL CCK-8 solution was added to each well and cells were then incubated at 37 °C for a further 2 h. The corresponding absorption at 450 nm was measured using a microplate reader to evaluate PTT efficiency.

Live/dead cell co-staining assay

4T1 cells were seeded into 35 mm confocal dishes (2 × 105 cells per dish) for 24 h and cocultured with PBS, TPE-Ni/OPYO NPs or TPE-Ni NPs for 12 h, respectively. Subsequently, the cells were washed three times with PBS and irradiated (940 nm, 1.0 W cm-2) for 5 min and further incubated for another 12 h. After that, the cells were co-incubated with both calcein AM (2 × 10−6 M) and propidium iodide (PI, 4 × 10−6 M) for 30 min in a humidified atmosphere containing 5% CO2 at 37 °C. The cells were washed three times with PBS and observed by CLSM.

Immunofluorescence assay

4T1 cells were grown in a confocal imaging dish at 37 °C. After the cells were incubated with PBS, TPE-Ni/OPYO NPs or TPE-Ni NPs (final TPE-Ni concentration is 40 μg mL-1, final OPYO concentration is 3.34 μg mL-1) for 12 h at 37 °C, the cells were washed and irradiated (940 nm, 1.0 W cm-2) for 5 min, the cells were further incubated at 37 °C for another 12 h. Then the cells were fixed with 4% paraformaldehyde for 15 min at room temperature, permeabilized with 0.2% Triton X-100 for 15 min at room temperature and then blocked with 5% skim milk in 0.2% PBS-T for 1 h. The cells were then incubated overnight at 4 °C with anti-calreticulin antibody (Abcam) followed by a further incubation at room temperature for 2 h with an Alexa Fluor® 488 secondary antibody (Abcam). Afterwards, the cells were stained with Hoechst 33342 for 15 min and subjected to CLSM analysis. Immunofluorescence staining experiments for HMGB1 were carried out using anti-HMGB1 antibody (Abcam) by the same method.

Establishment of 4T1 tumor models

All animal experiment protocols were approved by the Animal Ethics Committee of South China Agricultural University. A bilateral tumor mouse model was established through subcutaneous injection of 4T1 cells into the right and left hips of mice separately at -8 and -1 day before the treatments to develop the primary and distant tumors, respectively.

***In vivo* NIR fluorescence imaging**

NIR fluorescence imaging of mice was performed by a living imaging system. Fluorescence data were acquired with excitation and emission at 620 and 840 nm, respectively. Fluorescence images at 0 h were first captured before systemically administration of nanoparticles. The mice bearing xenograft 4T1 tumors were then administered with TPE-Ni/OPYO/TT-TBZ NPs (150 μL, the concentration of TPE-Ni = 250 μg mL-1, the concentration of OPYO = 21 μg mL-1) through tail vein injection (n = 3). Fluorescence intensity of mice were subsequently monitored at different time points (4, 6, 8, 10, 12, 24, and 48 h) post-injection of nanoparticles. Quantification of fluorescence was conducted by Living Image software.

***In vivo* biodistribution evaluation**

The mice bearing xenograft 4T1 tumors were then administered with TPE-Ni/OPYO/TT-TBZ NPs (150 μL, the concentration of TPE-Ni = 250 μg mL-1, the concentration of OPYO = 21 μg mL-1) through tail vein injection (n = 3). These mice were euthanized to extract heart, liver, spleen, lung, kidney and tumor at 6, 12 and 24 h post-injection timepoint. NIR fluorescence imaging of these tissues were conducted using an imaging system with excitation and emission wavelength at 620 and 840 nm, respectively. A Living Image software was used to analyze the captured images and measure the fluorescence intensity of tissues.

***In vivo* thermal imaging**

The mice bearing xenograft 4T1 tumors were then administered with PBS, TPE-Ni/OPYO NPs, TPE-Ni NPs (150 μL, the concentration of TPE-Ni = 250 μg mL-1 for TPE-Ni/OPYO NPs and TPE-Ni NPs, the concentration of OPYO = 21 μg mL-1 for TPE-Ni/OPYO NPs) through tail vein injection (n = 3). At t = 12 h, primary tumors of the mice were exposed under laser irradiation (940nm, 1.0 W cm-2) for 10 min. An IR thermal camera was used to measure the temperature changes of primary tumors.

***In vivo* assessments of synergistic antitumor effects**

A bilateral 4T1 tumor-bearing mouse model was established. The tumor bearing mice were randomly divide into six groups. The mice in each group were systemically administrated with 150 μL PBS, TPE-Ni/OPYO NPs or TPE-Ni NPs through tail-vein injection (the concentration of TPE-Ni = 250 μg mL^{-1} for TPE-Ni/OPYO NPs and TPE-Ni NPs, the concentration of OPYO = 21 μg mL^{-1} for TPE-Ni/OPYO NPs). At 12 h after administration, 940 nm laser irradiation was performed at

primary tumor site for 10 min at power intensity of 1.0 W cm^{-2}. During the whole treatment period, the volumes of both primary and distant tumors and the body weights of mice were monitored every 2 d. After 21 days of treatments, the mice in each group were euthanized, and both major organs (heart, liver, spleen, lung, and kidney) and tumors (primary tumors and distant tumors) were extracted for further studies. Tumor volumes (*V*) were calculated according to the following formula:

$$V = \frac{length_{tumor} \times (width_{tumor})^2}{2}$$

Histological analysis

After 21 days of treatments, tumors (primary tumors and distant tumors) were fixed in 4% paraformaldehyde. Then paraffin embedded sectioning was performed and hematoxylin and eosin (H&E) staining was carried out according to standard protocols. Images of slices were captured by an inverted microscope.

***In vivo* DC maturation evaluation**

A bilateral 4T1 tumor-bearing mouse model was established. The tumor bearing mice were randomly divide into six groups. The mice in each group were systemically administrated with 150 μL PBS, TPE-Ni/OPYO NPs or TPE-Ni NPs through tail-vein injection (the concentration of TPE-Ni = 250 μg mL-1 for TPE-Ni/OPYO NPs and TPE-Ni NPs, the concentration of OPYO = 21 μg mL-1 for TPE-Ni/OPYO NPs). At 12 h after administration, 940 nm laser irradiation was performed at primary tumor site for 10 min at power intensity of 1.0 W cm-2. After 3 days of treatment, mice in each group were euthanized and tumor-draining lymph nodes were extracted. The lymph nodes were homogenized into a single cell suspension in PBS solution, followed by staining with fluorophore-conjugated anti-CD45, anti-CD11b and anti-CD86 antibodies (Biolegend) according to the manufacture protocols. Stained cells are analyzed by a flow cytometry.

***In vivo* intratumoral T cell infiltration evaluation**

A bilateral 4T1 tumor-bearing mouse model was established. The tumor bearing mice were randomly divide into six groups. The mice in each group were systemically administrated with 150 μL PBS, TPE-Ni/OPYO NPs or TPE-Ni NPs through tail-vein injection (the concentration of TPE-Ni = 250 μg mL-1 for TPE-Ni/OPYO NPs and TPE-Ni NPs, the concentration of OPYO = 21 μg mL-1 for TPE-Ni/OPYO NPs). At 12 h after administration, 940 nm laser irradiation was performed at primary tumor site for 10 min at power intensity of 1.0 W cm-2. After 10 days of treatment, 4T1 tumor-bearing mice were euthanized to extract distant tumors. Single cell suspension solutions of tumors were collected followed by staining with fluorophore-conjugated anti-CD45, anti-CD3, anti-CD4, and anti-CD8 antibodies (Biolegend) according to the manufacture protocols. Stained cells are analyzed by a flow cytometry.

***In vivo* intrasplenic T cell population evaluation**

After 10 days of treatment, 4T1 tumor-bearing mice were euthanized to extract spleens. Single cell suspension solutions of tumors were collected followed by staining with fluorophore-conjugated anti-CD45, anti-CD3, anti-CD4, and anti-CD8 antibodies (Biolegend) according to the manufacture protocols. Stained cells are analyzed by a flow cytometry.

Evaluation of the number of NKT cells and serum cytokine levels in the blood

A bilateral 4T1 tumor-bearing mouse model was established. The tumor bearing mice were randomly divide into six groups. The mice in each group were systemically administrated with 150 μL PBS, TPE-Ni/OPYO NPs or TPE-Ni NPs through tail-vein injection (the concentration of TPE-Ni = 250 μg mL-1 for TPE-Ni/OPYO NPs and TPE-Ni NPs, the concentration of OPYO = 21 μg mL-1 for TPE-Ni/OPYO NPs). At 12 h after administration, 940 nm laser irradiation was performed at primary tumor site for 10 min at power intensity of 1.0 W cm-2. After 3 days of treatment, mice in each group were euthanized and the blood was collected. The lymphocytes in the blood were extracted according to the manufacture protocols. Single cell suspension solutions of lymphocytes were collected followed by staining with fluorophore-conjugated anti-CD45, anti-CD3, and anti-NK 1.1 antibodies (Biolegend) according to the manufacture protocols. Stained cells are analyzed by a flow cytometry. The residual blood was centrifuged and the serum was extracted. Subsequently, the corresponding Elisa kits were used to determine the IFN-γ, IL-6 and TNF-α in the serum according to the manufacture protocols.

***In vivo* biosafety evaluation of NPs**

After 21 days of treatment, the major organs (heart, liver, spleen, lung, and kidney) collected in the different treatment groups were for staining H&E staining. The long-term in vivo safety of TPE-Ni/OPYO NPs was evaluated in healthy female BALB/c mice (n = 5). Briefly, the mice were systematically administered with TPE-Ni/OPYO NPs by tail vein injection (the concentration of TPE-Ni = 250 μg mL-1, the concentration of OPYO = 21 μg mL-1). After 14 days of administration, the blood samples were collected from each mouse and used for blood routine analysis and biochemical analysis. The major organs (heart, liver, spleen, lung, and kidney) were collected for H&E staining.

Statistical Analysis

All data were presented as means ± standard deviation (SD). The results were analyzed by the Student's *t* test between two groups. The data were classified according to the p values and denoted by (*) for $p < 0.05$, (**) for $p < 0.01$, and (***) for $p < 0.001$.

Reporting summary

Further information on research design is available in the Nature Research Reporting Summary linked to this article.

Data availability

All the data supporting the findings of this study within the artile and its supplementary information are available from the corresponding author upon request.

References

1. Siegel R. L., Miller K. D., Fuchs H. E., Jemal A. Cancer statistics, 2022. *CA A Cancer J. Clin.* **72**, 7-33 (2022).
2. Conde J., Oliva N., Zhang Y., Artzi N. Local triple-combination therapy results in tumour regression and prevents recurrence in a colon cancer model. Nat. Mater. **15**, 1128-1138 (2016).
3. Petroni G., Cantley L. C., Santambrogio L., Formenti S. C., Galluzzi L. Radiotherapy as a tool to elicit clinically actionable signalling pathways in cancer. *Nat. Rev. Clin. Oncol.* **19**, 114-131 (2022).
4. Karges J., Yempala T., Tharaud M., Gibson D., Gasser G. A Multi-action and Multi-target RuII–PtIV Conjugate Combining Cancer-Activated Chemotherapy and Photodynamic Therapy to Overcome Drug Resistant Cancers. *Angew. Chem. Int. Ed.* **59**, 7069-7075 (2020).
5. De Ruysscher D., Niedermann G., Burnet N. G., Siva S., Lee A. W. M., Hegi-Johnson F. Radiotherapy toxicity. *Nat. Rev. Dis. Primers* **5**, 13 (2019).
6. Guo Z., et al. Radiotherapy-Induced Cleavage of Quaternary Ammonium Groups Activates Prodrugs in Tumors. *Angew. Chem. Int. Ed.* e202203444 (2022).
7. Feng B., Hou B., Xu Z., Saeed M., Yu H., Li Y. Self-Amplified Drug Delivery with Light-Inducible Nanocargoes to Enhance Cancer Immunotherapy. *Adv. Mater.* **31**, 1902960 (2019).

8. Gao S., Li T., Guo Y., Sun C., Xianyu B., Xu H. Selenium-Containing Nanoparticles Combine the NK Cells Mediated Immunotherapy with Radiotherapy and Chemotherapy. *Adv. Mater.* **32**, 1907568 (2020).
9. Wen M., Ouyang J., Wei C., Li H., Chen W., Liu Y. N. Artificial Enzyme Catalyzed Cascade Reactions: Antitumor Immunotherapy Reinforced by NIR-II Light. *Angew. Chem. Int. Ed.* **58**, 17425-17432 (2019).
10. Tan X., et al. Transformable Nanosensitizer with Tumor Microenvironment-Activated Sonodynamic Process and Calcium Release for Enhanced Cancer Immunotherapy. *Angew. Chem. Int. Ed.* **60**, 14051-14059 (2021).
11. Qi J., Ou H., Liu Q., Ding D.. Gathering brings strength: How organic aggregates boost disease phototheranostics. *Aggregate* **2**, 95-113 (2021).
12. Chen C., et al. Massively Evoking Immunogenic Cell Death by Focused Mitochondrial Oxidative Stress using an AIE Luminogen with a Twisted Molecular Structure. *Adv. Mater.* **31**, 1904914 (2019).
13. Huang L., et al. Mild photothermal therapy potentiates anti-PD-L1 treatment for immunologically cold tumors via an all-in-one and all-in-control strategy. *Nat. Commun.* **10**, 4871 (2019).
14. Ma Y., et al. Near-Infrared II Phototherapy Induces Deep Tissue Immunogenic Cell Death and Potentiates Cancer Immunotherapy. *ACS Nano* **13**, 11967-11980 (2019).
15. Liu C. C., Yang H., Zhang R., Zhao J. J., Hao D. J. Tumour-associated antigens and their anti-cancer applications. *Eur. J. Cancer* **26**, e12446 (2017).
16. Coulie P. G., Van den Eynde B. J., van der Bruggen P., Boon T. Tumour antigens recognized by T lymphocytes: at the core of cancer immunotherapy. *Nat. Rev. Cancer* **14**, 135-146 (2014).
17. Hessel C. M., et al. Copper Selenide Nanocrystals for Photothermal Therapy. *Nano Lett.* **11**, 2560-2566 (2011).
18. Lyu Y., Fang Y., Miao Q., Zhen X., Ding D., Pu K. Intraparticle Molecular Orbital Engineering of Semiconducting Polymer Nanoparticles as Amplified Theranostics for in Vivo Photoacoustic Imaging and Photothermal Therapy. *ACS Nano* **10**, 4472-4481 (2016).
19. Mu X., et al. Boost photothermal theranostics via self-assembly-induced crystallization (SAIC). *Aggregate* e170.
20. Ou G., Li Z., Li D., Cheng L., Liu Z., Wu H. Photothermal therapy by using titanium oxide nanoparticles. *Nano Res.* **9**, 1236-1243 (2016).
21. Xi D., et al. NIR Light-Driving Barrier-Free Group Rotation in Nanoparticles with an 88.3% Photothermal Conversion Efficiency for Photothermal Therapy. *Adv. Mater.* **32**, e1907855 (2020).
22. Sweeney E. E., Cano-Mejia J., Fernandes R. Photothermal Therapy Generates a Thermal Window of Immunogenic Cell Death in Neuroblastoma. *Small* **14**, 1800678 (2018).
23. Antaris A. L., et al. Ultra-Low Doses of Chirality Sorted (6,5) Carbon Nanotubes for Simultaneous Tumor Imaging and Photothermal Therapy. *ACS Nano* **7**, 3644-3652 (2013).
24. Robinson J. T., et al. Ultrasmall Reduced Graphene Oxide with High Near-Infrared Absorbance for Photothermal Therapy. *J. Am. Chem. Soc.* **133**, 6825-6831 (2011).
25. Cheng R., Meng F., Deng C., Klok H. A., Zhong Z. Dual and multi-stimuli responsive polymeric nanoparticles for programmed site-specific drug delivery. *Biomaterials* **34**, 3647-3657 (2013).
26. Kim J., Kim J., Jeong C., Kim W. J.. Synergistic nanomedicine by combined gene and photothermal therapy. *Adv. Drug Deliv. Rev.* **98**, 99-112 (2016).
27. Sun H., Zhang Q., Li J., Peng S., Wang X., Cai R. Near-infrared photoactivated nanomedicines for photothermal synergistic cancer therapy. *Nano Today* **37**, 101073 (2021).
28. Wang Y., et al. Highly Penetrable and On-Demand Oxygen Release with Tumor Activity Composite Nanosystem for Photothermal/Photodynamic Synergetic Therapy. *ACS Nano* **14**, 17046-17062 (2020).
29. Zeng F., et al. Coordinating the Mechanisms of Action of Ferroptosis and the Photothermal Effect for Cancer Theranostics. *Angew. Chem. Int. Ed.* **61**, e202112925 (2022).
30. Saxon E., Bertozzi C. R. Cell Surface Engineering by a Modified Staudinger Reaction. *Science* **287**, 2007-2010 (2000).
31. Bednarek C., Wehl I., Jung N., Schepers U., Bräse S. The Staudinger Ligation. *Chem. Rev.* **120**, 4301-4354 (2020).
32. Wang J., et al. Oligo(p-phenyleneethynylene) Derivatives for Mitochondria Targeting in Living Cells through Bioorthogonal Reactions. *Chem. Mater.* **30**, 5544-5549 (2018).
33. Liu S., et al. A far-red hybrid voltage indicator enabled by bioorthogonal engineering of rhodopsin on live neurons. *Nat. Chem.* **13**, 472-479 (2021).
34. Loehr M. O, Luedtke N. W. A Kinetic and Fluorogenic Enhancement Strategy for Labeling of Nucleic Acids. *Angew. Chem. Int. Ed.* **61**, e202112931 (2022).
35. Yip A. M-H, Lai C. K-H, Yiu K. S-M, Lo K. K-W. Phosphorogenic Iridium(III) bis-Tetrazine Complexes for Bioorthogonal Peptide Stapling, Bioimaging, Photocytotoxic Applications, and the Construction of Nanosized Hydrogels. *Angew. Chem. Int. Ed.* **61**, e202116078 (2022).
36. Burke E. G., Gold B., Hoang T. T., Raines R. T., Schomaker J. M. Fine-Tuning Strain and Electronic Activation of Strain-Promoted 1,3-Dipolar Cycloadditions with Endocyclic Sulfamates in SNO-OCTs. *J. Am. Chem. Soc.* **139**, 8029-8037 (2017).
37. Kim E., Koo H. Biomedical applications of copper-free click chemistry: in vitro, in vivo, and ex vivo. *Chem. Sci.* **10**, 7835-7851 (2019).
38. Lefebvre J., Guetta C., Poyer F., Mahuteau-Betzer F., Teulade-Fichou M.-P. Copper–Alkyne Complexation Responsible for the Nucleolar Localization of Quadruplex Nucleic Acid Drugs Labeled by Click Reactions. *Angew. Chem. Int. Ed.* **56**, 11365-11369 (2017).
39. Wang S., et al. Quinoline-Based Photolabile Protection Strategy Facilitates Efficient Protein Assembly. *J. Am. Chem. Soc.* **144**, 1232-1242 (2022).
40. Haase C., Rohde H., Seitz O. Native Chemical Ligation at Valine. *Angew. Chem. Int. Ed.* **47**, 6807-6810 (2008).
41. Hu R., et al. Lab-in-cell based on spontaneous amino-yne click polymerization. *Sci. China Chem.* **62**, 1198-1203 (2019).
42. Zhu X., Li J., Qiu X., Liu Y., Feng W., Li F. Upconversion nanocomposite for programming combination cancer therapy by precise control of microscopic temperature. *Nat. Commun.* **9**, 2176 (2018).
43. Ahmadi S., et al. Stimulus-responsive sequential release systems for drug and gene delivery. *Nano Today* **34**, 100914 (2020).
44. Sun T., Zhang Y. S., Pang B., Hyun D. C., Yang M., Xia Y.. Engineered Nanoparticles for Drug Delivery in Cancer Therapy. *Angew. Chem. Int. Ed.* **53**, 12320-12364 (2014).
45. Zheng M., et al. Robust ICG Theranostic Nanoparticles for Folate Targeted Cancer Imaging and Highly Effective Photothermal Therapy. *ACS Appl. Mater. Interfaces* **6**, 6709-6716 (2014).
46. Bi S., Deng Z., Jiang Q., Jiang M., Zeng S.. A H_2S-Triggered Dual-Modal Second Near-Infrared/Photoacoustic Intelligent Nanoprobe for Highly Specific Imaging of Colorectal Cancer. *Anal. Chem.* **93**, 13212-13218 (2021).
47. Galluzzi L., Buqué A., Kepp O., Zitvogel L., Kroemer G. Immunogenic cell death in cancer and infectious disease. *Nat. Rev. Immunol.* **17**, 97-111 (2017).
48. Duan X., Chan C., Lin W.. Nanoparticle-Mediated Immunogenic Cell Death Enables and Potentiates Cancer Immunotherapy. *Angew. Chem. Int. Ed.* **58**, 670-680 (2019).
49. Tu Y., Zhao Z., Lam J. W. Y., Tang B. Z. Mechanistic connotations of restriction of intramolecular motions (RIM). *Nati. Sci. Rev.* **8** (2021).

50. Gao A., et al. Sheddable Prodrug Vesicles Combating Adaptive Immune Resistance for Improved Photodynamic Immunotherapy of Cancer. *Nano Lett.* **20**, 353-362 (2020).
51. Woo S. R., Corrales L., Gajewski T. F. Innate Immune Recognition of Cancer. *Annu. Rev. Immunol.* **33**, 445-474 (2015).
52. Yu Y., et al. Polymeric PD-L1 blockade nanoparticles for cancer photothermal-immunotherapy. *Biomaterials* **280**, 121312 (2022).
53. Bennstein S. B. Unraveling Natural Killer T-Cells Development. *Front. Immunol.* **8** (2018).
54. Vivier E, Ugolini S, Blaise D, Chabannon C, Brossay L. Targeting natural killer cells and natural killer T cells in cancer. *Nat. Rev*. *Immunol*. **12**, 239-252 (2012).

Acknowledgements

A This work was financially supported by the National Natural Science Foundation of China (21788102 and 21907034), the Natural Science Foundation of Guangdong Province (Grant Nos. 2019B030301003 and 2016A030312002), the National Key Research and Development Program of China (Intergovernmental cooperation project, Grant No. 2017YFE0132200), and the Innovation and Technology Commission of Hong Kong (Grant No. ITC−CNERC14S01).

Author contributions

These authors contributed equally: Guiquan Zhang, Xuemei Chen. Guiquan Zhang: Conceptualization, Methodology, Investigation, Writing manuscript. Xuemei Chen: Investigation (synthesizing the compound TPE-Ni) and revised the manuscript. Xu Chen: Investigation (synthesizing the compound OPYO). Kaihong Du and Dong He: Investigation (providing the assistance for *in vivo* experiments). Keke Ding: Investigation (providing the assistance for data analyzing). Dan Ding: Investigation. Rong Hu: Conceptualization, Supervision, Writing – review & editing. Anjun Qin: Conceptualization, Supervision, Writing – review & editing, Project administration, Funding acquisition. Ben Zhong Tang: Supervision, Funding acquisition.

Conpeting Interests

The authors declare no conflict of interest.

Keywords: synergistic treatment • photothermal immunotherapy • chemotherapy • immunogenic cell death • immunotherapy

Entry for the Table of Contents

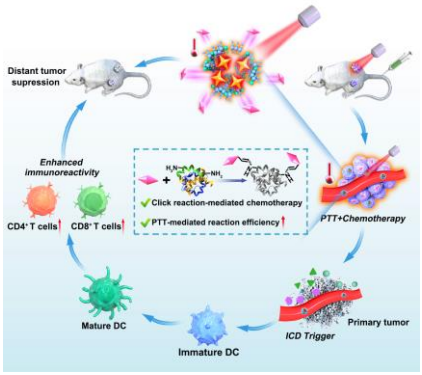

Photothermally responsive nanoparticles featuring the synergetic photothermal therapy and click reaction-mediated chemotherapy for enhanced tumor immunotherapy were constructed. Under NIR laser irradiation, ICD of primary tumors is activated by TPE-Ni-based photothermal therapy and further enhanced by click reation-based chemotherapy, leading to the inhibition of both primary and distant tumor. This strategy provides a promising platform for enhancing immunotherapy of tumor treatments.